

Article

A dislocation-scale characterization of the evolution of deformation microstructures around nanoindentation imprints in a TiAl alloy

Antoine Guitton ^{1,2,*}, Hana Kriaa ^{1,2}, Emmanuel Bouzy ^{1,2}, Julien Guyon ^{1,2} and Nabila Maloufi ^{1,2}

¹ Laboratoire d'Étude des Microstructures et de Mécanique des Matériaux (LEM3) – UMR CNRS 7239 – Université de Lorraine, 7 rue Félix Savart, BP 15082, 57073 Metz Cedex 3, France

² Laboratory of Excellence on Design of Alloy Metals for low-mAss Structures (DAMAS) – Université de Lorraine, France

* Correspondence: antoine.guitton@univ-lorraine.fr; Tel.: +33-372-747-787

Abstract: In this work, plastic deformation was locally introduced at room temperature by nanoindentation on a γ -TiAl based alloy. Comprehensive analyzes of microstructures were performed before and after deformation. In particular, the Burgers vectors, the line directions and the mechanical twinning systems were studied via accurate electron channeling contrast imaging. Accommodation of the deformation are reported and a scenario is proposed. All features help to explain the poor ductility of the TiAl based alloys at room temperature.

Keywords: TiAl alloys, dislocation, twinning, nanoindentation, ECCI

1. Introduction

Titanium aluminide alloys have attracted considerable attention due to their unique combination of properties such as high specific strength and stiffness, good creep properties and resistance against oxidation and corrosion [1] [2], which make them suitable candidate materials for High Temperature (HT) applications [3] [4].

One of the main weaknesses of TiAl alloys is that they are brittle at Room Temperature (RT), *i.e.* below their brittle-to-ductile transition temperature, which lies between 800°C and 1000°C [5]. Despite intense research on the HT behavior of TiAl alloys, literature suffers from a lack of understanding on their RT behavior particularly on the elementary deformation mechanisms and the precise role of microstructures [6] [7] [8].

Among the several Ti-Al alloy phases, two of them are ordered at RT [4]: γ as the major phase and α_2 as a minor phase. The α_2 phase is hexagonal ($\frac{c}{a} = 0.8$) with a DO19 structure while the γ phase is tetragonal with a L1₀ structure close to cubic ($\frac{c}{a} = \frac{c}{b} = 1.02$). Therefore, six order variants are possible.

They can be visualized as generated by a 120° rotation around the $(1\ 1\ 1)$ plane normal [9].

The microstructures of γ -TiAl alloys are complex. A good compromise for balancing properties between RT plasticity, high strength and good creep resistance at HT can be obtained for the duplex microstructure. It is constituted of a mixture of monolithic γ grains and small lamellar colonies of γ and α_2 [10] [11].

In dual-phase TiAl alloys, plastic deformation mainly occurs on the $\{111\}$ planes of the γ phase by dislocation glide or twinning. It is strongly related to the ordered $L1_0$ structure [12]: along the $\langle\bar{1}10\rangle$ -directions, there is only one sort of atoms (Ti or Al). In this case, dislocations are called ordinary dislocations, and their Burgers vectors are $\frac{1}{2}\langle110\rangle$ types. Because Ti-atoms and Al-atoms interchange in $\langle011\rangle$ -directions, the $\langle11\bar{2}\rangle$ and the $\langle101\rangle$ dislocations are called superdislocations. These two types of superdislocations can undergo various dissociations into superpartials *i.e.* partial dislocations with the associated planar faults. In addition, true twinning along $\frac{1}{6}\langle11\bar{2}\rangle\{111\}$ occurs that does not alter the ordered $L1_0$ structure of the γ -TiAl. Because of the specific structure of the γ -TiAl, it is relatively easy to know the direction for either slip of ordinary dislocations or for true twinning when the slip/twin plane is known [12]. Note also that at RT twinning and then glide of ordinary dislocations are the easiest deformation modes [2] [7] [8]. In this manner, Kauffmann *et al.* suggested that increasing deformation leads to the nucleation of only a few new mechanical twins since the dislocation movement becomes more dominant with increasing strain [8].

Although it is accepted that the α_2 phase does not contribute to the deformation [6] [12], evidences of prismatic slip $\langle1\bar{2}10\rangle\{10\bar{1}0\}$, basal slip $\langle1\bar{2}10\rangle(0001)$ and pyramidal slip $\langle11\bar{2}\bar{6}\rangle\{1\bar{2}11\}$ were reported [12].

Among the difficulties encountered for understanding the mechanical behavior of TiAl based alloys, most of our detailed knowledge on their deformation mechanisms has been deduced from Transmission Electron Microscopy (TEM) observations on an electron transparent lamella [13] [7]. The investigation presented in this article focuses on the study of deformation mechanisms at the mesoscopic scale. With an original combination of experiments, we investigate the evolution of deformation microstructures at RT in the γ phase of a dual-phase bulk TiAl alloy. Because of the RT brittleness of this material, plastic deformation is induced by nanoindentation. The solid confinement around the indent maintains the integrity of the sample, while applying the load. Note also, that nanoindentation is a surface technique, so that the stress state at the specimen surface is different to that in the volume. The evolution of the microstructures is characterized by accurate Electron Channeling Contrast Imaging (aECCI) before and after deformation.

2. Materials and Methods

The fully dense Ti-46.8Al-1.7Cr-1.8Nb (at.%) sample was obtained in the form of investment cast-bars (diameter 15 mm, height 230 mm) from Howmet. The as-received bars were hot isostatically pressed at 1250°C and 125 MPa for 4 hours, then subjected to a homogenization treatment in a furnace under vacuum at 1270°C for 24 hours [14]. Then the sample was ground using silicon carbide paper and then polished with a 1 μ m diamond suspension. Finally, in order to produce a very flat surface

and to avoid any work hardening due to conventional grinding, a chemo-mechanical polishing has been performed using a colloidal silica suspension.

Because deformation occurs mainly in the γ -phase [5], plastic deformation was locally introduced on the γ phase by nanoindentation using the Ultra Nanoindentation Tester from Anton Paar (Switzerland), equipped with a Berkovich indenter. The indents were organized in a regular array of 500 μN indents. For easier recognition, it was surrounded by 20 mN indents away at few hundreds of μm .

Detailed characterizations of microstructures before and after deformation were performed by aECCI using a Zeiss Auriga Scanning Electron Microscope (SEM) operating at 10 kV. aECCI is a non-destructive method offering the ability to provide, inside a SEM, TEM-like diffraction contrast imaging of sub-surface defects (at a depth of about one hundred of nanometers) on centimetric bulk specimen. Defects, such as dislocations, can be characterized by applying the TEM extinction criteria [15] [16]. Because the yield of BSE depends drastically on the orientation of the crystal relative to the incident electron beam *i.e.* optic axis of the SEM, obtaining the crystallographic orientation of the grain of interest with an accuracy of 0.1° is a preliminary step to aECCI [16]. The precise orientation of the crystal in the SEM coordinate system is given through Selected Area Channeling Pattern (SACP). To overcome this challenge, rocking the incident electron beam at a pivot point on the surface of a given grain of the sample provides High-Resolution Selected Channeling Patterns (HR-SACP) [17]. HR-SACP cover an angular range of 4.4° and reach an accuracy for the orientation better than 0.1° with a spatial resolution less than 500 nm. Because of this small angular range, for getting the orientation of the grain of interest, the HR-SACP is superimposed on an Electron BackScattered Diffraction (EBSD) pattern simulated at 0° using "Esprit DynamicS" software from Bruker. Note that, the reason for using an EBSD pattern (acquired at 70°) simulated at 0° is that the specimen is initially placed at 0° for aECCI.

EBSD experiments were carried out on a Zeiss Supra 40 SEM operating at 20 kV. In order to discriminate the different order variants of γ -TiAl, fine EBSD analyses were performed at a step of 75 nm with Channel 5 as the indexation software.

3. Results

3.1. Characterization of the microstructure around the regions of interest

Figure 1.(a) and **Figure 1.(b)** show the microstructure around the Regions of Interest (ROI): ROI1 on grain A away from any interfaces and ROI2 over both grains A and B. ROI1 and ROI2 are presented in **Figure 2** and **Figure 3** respectively. Note that, references [18] and [19] mentioned that interfaces play an important role in TiAl alloys, thus controlling the yield stress.

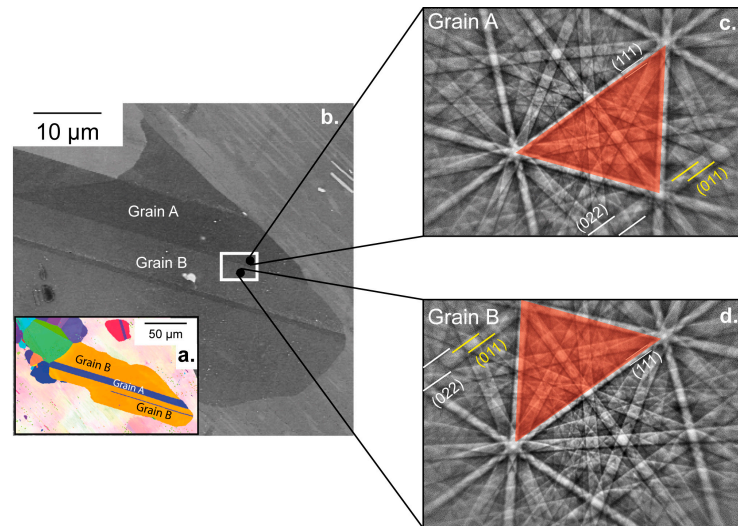


Figure 1. (a) EBSD orientation map of the zone of interest. (b) Enhanced BSE image showing the microstructure before deformation. The nanoindentation array is localized in the white rectangle. (c) and (d) EBSD patterns corresponding to grains A and B.

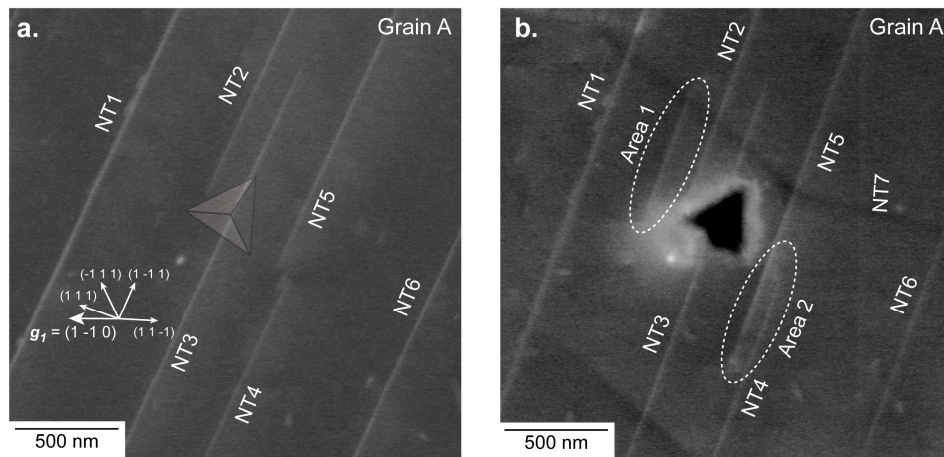


Figure 2. ROI1 for which the surface is close to $(4 \ 5 \ 7)$. (a) aECCI obtained with $g_1 = (1 \ 1 \ 0)$ showing six $[1 \ 1 \ 2](1 \ 1 \ 1)$ Nano-Twins (NT) and the position of the imprint (transparent Berkovich imprint). The white arrows indicate the trace of the $\{1 \ 1 \ 1\}$ planes. (b) Enhanced BSE image showing the 500 μN indent. Two areas (labelled Area 1 and 2) have changed. The NT7 slightly visible in (b) comes from a neighbor imprint.

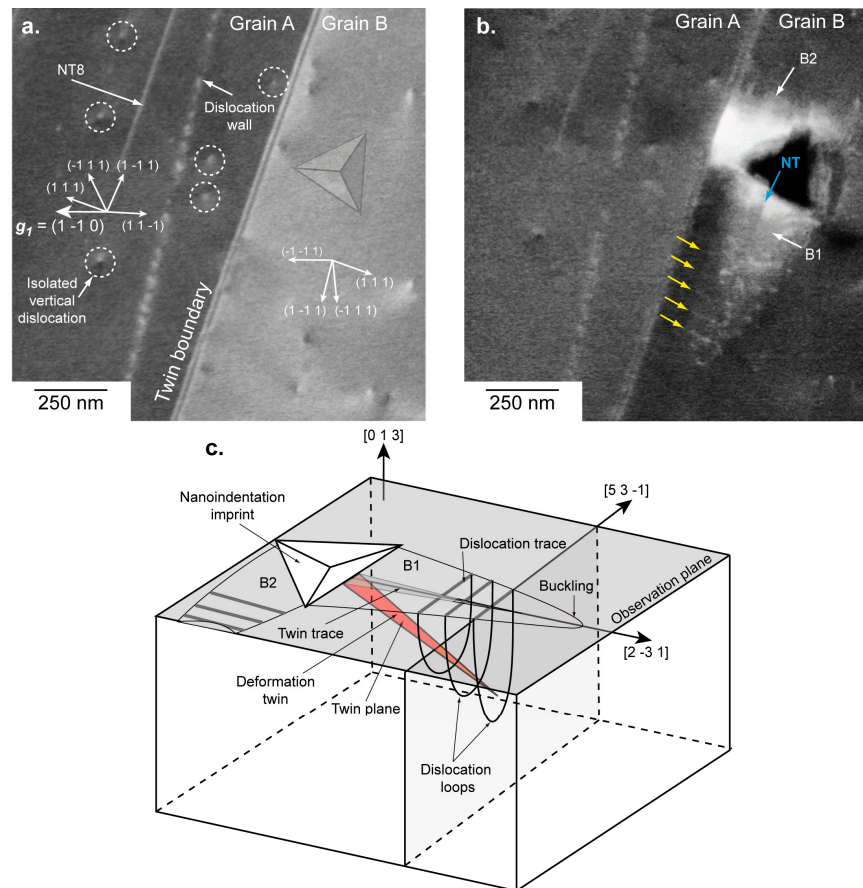


Figure 3. ROI2, where the surface plane is near $(4\ 5\ 7)$ for the twin A (left) and near $(0\ 1\ 3)$ for grain B. The TB corresponds to the $[1\ 1\ 2](1\ 1\ 1)$ system. (a) aECCI obtained with $\mathbf{g}_1 = (1\ \bar{1}\ 0)$ with the transparency position of the Berkovich imprint. The white arrows indicate the trace of the $\{1\ 1\ 1\}$ planes. (b) Enhanced BSE image showing two buckling areas (labelled B1 and B2) clearly visible around the 500 μN indent. The blue arrow points to a NT and the yellow to dislocations. (c) 3D schematic of B1 and B2.

Experimentally, the twin nature (true or pseudo twin) is determined using the high-resolution spot mode EBSD. Patterns are collected by manually pointing the electron beam at both sides of the Twin Boundary (TB). The corresponding EBSD patterns (**Figure 1.(c)** and **Figure 1.(d)**) clearly indicate that the grains A and B are true twin related: for example, the red triangle formed by the 3 bands depicted in **Figure 1.(c).(d)** and the $(0\ 1\ 1)$ superlattice band are in symmetrical position with respect to the unchanged $(1\ 1\ 1)$ band when going from grain A to grain B.

The evolution of the ROI1, before and after deformation, is presented on **Figure 2.(a)** (ECC image) and **Figure 2.(b)** (BSE micrograph). Due to a rapid contamination of the sample surface under the electron beam, controlling the channeling conditions after deformation with the required accuracy for aECCI was not possible. However, enhanced BSE images were acquired and bring the necessary information for understanding the evolution of the microstructure already fully characterized before deformation.

EBSD gives $(42\ 54\ 73) \sim (4\ 5\ 7)$ as surface plane so that seven channeling conditions or diffracting vectors \mathbf{g} are accessible by tilting and rotating the specimen: $\mathbf{g}_1 = (1\ \bar{1}\ 0)$, $\mathbf{g}_2 = (1\ 1\ \bar{1})$, $\mathbf{g}_3 = (3\ \bar{1}\ \bar{1})$, $\mathbf{g}_4 = (3\ \bar{3}\ 1)$, $\mathbf{g}_5 = (1\ 3\ \bar{3})$, $\mathbf{g}_6 = (1\ \bar{3}\ 1)$, $\mathbf{g}_7 = (4\ 0\ \bar{2})$ (note that only the ECC image taken with \mathbf{g}_1 is shown in **Figure 2.(a)**). In such conditions, all defects are expected to be in contrast. Neither dislocation nor superdislocation are observed before deformation in **Figure 2.(a)**. Only parallel linear contrasts (labelled NT) are clearly visible. In addition, they are aligned along the $\sim [2\ \bar{3}\ 1]$ direction. Such BSE contrast is generally attributed to Nano-Twins (NT) and is consistent with $[1\ 1\ \bar{2}](1\ 1\ 1)$ as true twin system [20] [21] [22]. After deformation (see **Figure 2.(b)**), no dislocation is visible, but changes clearly identifiable are localized in the vicinity of the indent (Area 1 and Area 2 in **Figure 2.(b)**). In Area 1, near the imprint, a $[1\ 1\ \bar{2}](1\ 1\ 1)$ deformation NT was created. At the other side of the imprint (Area 2) the NT5 extends along the $\sim [2\ \bar{3}\ 1]$. Note that the NT7 visible in **Figure 2.(b)** comes from a neighbor imprint.

3.3 Microstructure evolution of the ROI2

ROI2 is composed by two twinned grains A (left) and B (right) with their surface plane as $(42\ 54\ 73) \sim (4\ 5\ 7)$ and $(16\ 325\ 946) \sim (0\ 1\ 3)$ respectively (see **Figure 3.(a)**). The common direction on the sample surface for both grains A and B is $[2\ \bar{3}\ 1]$. The $\{1\ 1\ 1\}$ -plane, which intercepts both the $(4\ 5\ 7)$ plane and the $(0\ 1\ 3)$ plane along $[2\ \bar{3}\ 1]$ is the $(1\ 1\ 1)$. Note also that a NT aligned along $\sim [2\ \bar{3}\ 1]$ is visible (labelled NT8 in **Figure 3**) and consistent with $[1\ 1\ \bar{2}](1\ 1\ 1)$. The vertical dislocations (*i.e.* almost perpendicular to the sample surface) either isolated or stacked into a wall in grain A (**Figure 3.(a)**) are analyzed by aECCI in order to determine their Burgers vectors. Using the diffracting conditions \mathbf{g}_1 to \mathbf{g}_7 previously mentioned with invisibility criteria leads to $\pm \frac{1}{2}[1\ 1\ 0]$ as the Burgers vector.

Unfortunately good channeling conditions are not reachable in the right $(0\ 1\ 3)$ grain, resulting in the non-characterization of the isolated vertical dislocations. **Figure 3.(b)** and its schematic show the ROI2 after deformation. The 500 μN indent was made in the $(0\ 1\ 3)$ grain near the TB. Around this indent, two similar features (labelled B1 and B2 in **Figure 3.(b)**) are observed. Parallel to the TB *i.e.* in B1, a set of parallel dislocation traces is visible (yellow arrows in **Figure 3.(b)**). They are localized in an elliptical area forming a buckling (B1) extending far away

from the imprint in the $[2\bar{3}1]$ direction. Such buckling areas were already reported but not explained for TiAl alloys [18] [23].

In addition, a NT contrast (blue arrow in **Figure 3.(b)**) is observed inside B1, and it is parallel to $[2\bar{3}1]$ consistent with the $[1\bar{1}\bar{2}](111)$ true twinning system.

Perpendicular to the TB *i.e.* along $[\bar{5}\bar{3}1]$, another buckling area B2 is observed, and it cannot extend because it is blocked by the TB. In the neighbor (457) grain, no change is observed compared to the initial state, even if the TB is distorted locally where B2 is in contact. Outside both buckling areas, no other defect is observed.

4. Discussion

From observations of the evolution of microstructures of ROI1, two assessments can be made:

1. at RT, twinning is observed to be the main deformation mechanism, in agreement with literature [2] [7] [8]. But contrary to Zambaldi *et al.*, who prefer to suggest that ordinary dislocation glide is the main deformation mechanism at RT (without totally excluding twinning) from observations by atomic force microscopy around high load (3000 μN) imprints [18].
2. deformation is observed to be localized near the indent.

In many materials, buckling areas such as those characterized in ROI2 are associated with a canalization of the deformation, generally taking its origin from the accommodation of twins [24]. Although the accommodation of $\frac{1}{6}[1\bar{1}\bar{2}]\{111\}$ twin by $\frac{1}{2}[1\bar{1}0]\{111\}$ ordinary dislocations was already reported by TEM experiments in TiAl alloys [25] [26], no mechanism was proposed.

From this knowledge, and taking into account our results, we propose the following scenario (see **Figure 3.(c)**):

- Under the indent, the $[1\bar{1}\bar{2}](111)$ NT is formed.
- The stress concentration at the tip of the $[1\bar{1}\bar{2}](111)$ NT nucleates ordinary $\pm\frac{1}{2}[1\bar{1}0]$ dislocation loops gliding in the $(1\bar{1}1)$ planes. The dislocation loops will form an ellipsoid surrounding the NT thus producing lines after projection on the observation plane.
- The elliptical area or B1 will grow by adding successive dislocation loops at its extremity.
- B1 will extend until it will meet an obstacle such as the TB (for B2 for example).
- At the location where B2 intercepts the TB, a stress concentration appears. It results in a local distortion of the boundary. Therefore the TB seems to be a strong obstacle to the propagation of the deformation and at higher load it may cause microcracking at its vicinity as observed in references [18] [26] [27].

Furthermore, we can suggest that the low load used (500 μN) is just high enough for generating a complex and non-uniaxial stress field at the tip of the indent. This leads to the activation of the main deformation mechanism *i.e.* twinning, but it is too low for dislocation glide. For higher loads, both mechanisms are activated subsequently, and lead to the formation of a buckling area, according to the previous scenario.

199 5. Conclusions

200 In summary, RT nanoindentation tests combine with aECCI observations before and after
201 deformation bring novel insights into the γ -TiAl deformation mechanisms:

- 202 1. At RT, twinning is observed to be the main deformation mechanism.
- 203 2. Twinning is accommodated by ordinary dislocation mechanism leading to the canalization of
204 the deformation.
- 205 3. TB can play the role of obstacle to the propagation of deformation to neighbor grains leading to
206 a stress concentration at the vicinity of the boundary. Therefore, the true twin seems to be one of the
207 weak links explaining the poor ductility of γ -TiAl at RT.

208

209

210 **Acknowledgments:** The author thank Dr. N. Gey from the LEM3 for discussions.

211 **Author Contributions:** All experimental observations were performed by HK and AG. AG and HK performed
212 the dislocation analyses. AG wrote the main manuscript. All the authors participate in the discussion and they
213 reviewed the manuscript.

214 **Conflicts of Interest:** The authors declare no conflict of interest.

215

References

- [1] Kim, Y.; Dimiduk, D. Progress in the understanding of gamma titanium aluminides, *JOM* **1991**, 43, pp. 40-47, doi: 10.1007/BF03221103.
- [2] Appel, F.; Wagner, R. Microstructure and deformation of two-phase gamma-titanium aluminides. *Mater. Sc. Eng. R* **1998**, 22, pp. 187-268, doi:10.1016/S0927-796X(97)00018-1
- [3] Loria, E. Quo vadis gamma titanium aluminide. *Intermetallics* **2001**, 9, pp. 997-1001, doi: 10.1016/S0966-9795(01)00064-4.
- [4] Schuster, J.; Palm, M. Reassessment of the binary aluminum-titanium phase diagram. *J. Phase Equilib. Diff* **2006**, 27, pp. 255-277, doi: 10.1361/154770306X109809.
- [5] Zambaldi, C. Micromechanical modeling gamma-TiAl based alloys. RWTH Aachen University, Aachen, 2010; 978-3-8322-9717-6.
- [6] Appel, F.; Paul, D.; Oehring, M. Gamma titanium aluminide alloys: science and technology, Wiley-VCH Verlag GmbH, 2011; 9783527315253.
- [7] Beran, P.; Heczko, M.; Kruml, T.; Panzner, T.; Van Petegem, S. Complex investigation of deformation twinning in γ -TiAl by TEM and neutron diffraction. *J. Mech. Phys. Sol* **2016**, 95, pp. 647-662, doi: 10.1016/j.jmps.2016.05.004.
- [8] Kauffmann, F.; Bidlingmaier, T.; Dehm, G.; Wanner, A.; Clemens, H. On the origin of acoustic emission during room temperature compressive deformation of a gamma-TiAl based alloy. *Intermetallics* **2000**, 8, pp. 823-830, doi: 10.1016/S0966-9795(00)00025-X
- [9] Zambaldi, C.; Zaefferer, C.; Wright, S. Characterization of order domains in γ -TiAl by orientation microscopy based on electron backscatter diffraction. *App. Crystal* **2009**, 42, pp. 1092-1101, doi: 10.1107/S0021889809036498.
- [10] Dey, S.; Hazotte, A.; Bouzy, E. Multiscale gamma variant selection in a quaternary near-gamma Ti-Al alloy. *Philos. Mag* **2006**, 2006, no. 86, pp. 3089-3112, doi: 10.1080/14786430600669832.
- [11] Dey, S.; Morawiec, A.; Bouzy, E.; Hazotte, A.; Fundenberger, J.-J. Determination of gamma/gamma interface relationships in a (α_2 + gamma) TiAl base alloy using TEM Kikuchi patterns obtained by nanoprobe scanning. *Mater. Lett* **2003**, 60, pp. 646-650, doi: 10.1016/j.matlet.2005.09.052.
- [12] Marketz, M.; Fischer, F.; Clemens, H. Deformation mechanisms in TiAl intermetallics - experiments and modeling. *Int. J. Plasticity* **2003**, 19, pp. 281-321, doi: 10.1016/S0749-6419(01)00036-5.
- [13] Zghal, S.; Coujou, A.; Couret, A. Transmission of the deformation through γ - γ interfaces in a polysynthetically twinned TiAl alloy. *Philos. Mag* **2001**, 81, pp. 345-382, doi: 10.1080/01418610108214308.
- [14] Dey, S.; Hazotte, A.; Bouzy, E.; Naka, S. Development of Widmanstätten laths in a near-gamma TiAl alloy. *Acta Mater* **2005**, 53, pp. 3783-3794, doi: 10.1016/j.actamat.2005.04.007
- [15] Mansour, H.; Guyon, J.; Crimp, M.; Gey, N.; Beausir, B.; Maloufi, N. Accurate electron channeling contrast analysis of dislocations in fine grained bulk materials. *Scr. Mater* **2014**, 84-85, pp. 11-14, doi: 10.1016/j.scriptamat.2014.03.001.
- [16] Kriaa, H.; Guitton, A.; Maloufi, N. Fundamental and experimental aspects of diffraction for characterizing dislocations by electron channeling contrast imaging in scanning electron microscope. *Sc. Rep* **2017**, p. in press, doi: 10.1038/s41598-017-09756-3

- 257 [17] Guyon, J.; Mansour, H.; Gey, N.; Crimp, M.; Chalal, S.; Maloufi, N. Sub-micron resolution selected
258 area electron channeling patterns. *Ultramicro* **2015**, *149*, pp. 34-44, doi: 10.1016/j.ultramicro.2014.11.004
- 259 [18] Zambaldi, C.; Raabe, D. Plastic anisotropy of gamma-TiAl revealed by axisymmetric indentation.
260 *Acta Materialia* **2010**, *58*, pp. 3516-3530, doi: 10.1016/j.actamat.2010.02.025
- 261 [19] Kad, B.; Asaro, R.J. Apparent Hall-Petch effects in polycrystalline lamellar TiAl. *Philos. Mag. A*
262 **2006**, *75*, no. 1, pp. 87-104, doi: 10.1080/01418619708210284
- 263 [20] Simki, B.; Ng, B.; Crimp, M.; Bieler, T. Crack opening due to deformation twin shear at grain
264 boundaries in near- γ TiAl. *Intermetallics* **2007**, *15*, pp. 55-60, doi: 10.1016/j.intermet.2006.03.005
- 265 [21] Simki, B.; Crimp, M.; Bieler, T. A factor to predict microcrack nucleation at γ - γ grain boundaries
266 in TiAl. *Scripta Mat* **2003**, *49*, pp. 149-154, doi: 10.1016/j.intermet.2006.03.005
- 267 [22] Ng, B.; Simki, B.; Crimp, M.; Bieler, T. The role of mechanical twinning on microcrack
268 nucleation and crack propagation in a near- γ TiAl alloy. *Intermetallics* **2004**, *12*, pp. 1317-1323, doi:
269 10.1016/j.intermet.2004.03.015.
- 270 [23] Gehard, S.; Pyczak, F.; Göken, M. Microstructural and micromechanical characterisation of TiAl
271 alloys using atomic force microscopy and nanoindentation. *Materials Science and Engineering A*
272 **2009**, *523*, pp. 235-241, doi: 10.1016/j.msea.2009.05.068.
- 273 [24] Hirth, J. P.; Lothe, J. *Theory of dislocations*, 2nd ed.; Krieger Publishing Company, 1982, pp 756;
274 0521864364.
- 275 [25] Gibson, M.; Forwood, C. Slip transfer of deformation twins in duplex γ -based Ti-Al alloys: Part
276 III. Transfer across general large-angle γ - γ grain boundaries. *Philos. Mag. A* **2002**, *82*, no. 7, pp. 1381-
277 1404, doi: 10.1080/01418610208235678
- 278 [26] Simki, B.; Crimp, M.; Bieler, T. A factor to predict microcrack nucleation at gamma-gamma grain
279 boundary in TiAl. *Scr. Mater* **2003**, *49*, pp. 149-154, doi : 10.1016/S1359-6462(03)00216-1
- 280 [27] Bieler, T.; Fallahi, A.; Ng, B.; Kumar, D. Crimp, M.; Simki, B.; Zamiri, A.; Pourboghrat, F.; Mason,
281 D. Fracture initiation/propagation parameters for duplex TiAl grain boundaries based on twinning,
282 slip, crystal orientation and boundary misorientation. *Intermetallics* **2005**, *13*, pp. 979-984, doi:
283 10.1016/j.intermet.2004.12.013.